Equations of state in a lattice Boltzmann model

Peng Yuan and Laura Schaefer

Articles you may be interested in

On One-dimensional Discrete Velocity Models of The Boltzmann Equation For Mixtures
AIP Conf. Proc. **762**, 120 (2005); 10.1063/1.1941524

Nanoscale air bearing modeling via lattice Boltzmann method
J. Appl. Phys. **97**, 10P304 (2005); 10.1063/1.1852333

A Look at Lattice Boltzmann Equations: The Lattice Boltzmann Equation: For Fluid Dynamics and Beyond
Comput. Sci. Eng. **5**, 86 (2003); 10.1109/MCISE.2003.1182967

Applying the Lattice Boltzmann Equation to Multiscale Fluid Problems
Comput. Sci. Eng. **3**, 26 (2001); 10.1109/5992.963425

Lattice Boltzmann modeling of interfacial gravity waves
Phys. Fluids **10**, 1490 (1998); 10.1063/1.869669

Equations of state in a lattice Boltzmann model

Peng Yuan[a] and Laura Schaefer
Department of Mechanical Engineering, University of Pittsburgh, Pittsburgh, Pennsylvania 15261

In this paper we consider the incorporation of various equations of state into the single-component multiphase lattice Boltzmann model. Several cubic equations of state, including the van der Waals, Redlich-Kwong, and Peng-Robinson, as well as a noncubic equation of state (Carnahan-Starling), are incorporated into the lattice Boltzmann model. The details of phase separation in these nonideal single-component systems are presented by comparing the numerical simulation results in terms of density ratios, spurious currents, and temperature ranges. A comparison with a real fluid system, i.e., the properties of saturated water and steam, is also presented. © *2006 American Institute of Physics.*
[DOI: 10.1063/1.2187070]

I. INTRODUCTION

Recently, the lattice Boltzmann equation (LBE) method has emerged as an alternative way of simulating fluid flow and transport phenomena.[1,2] Differing from conventional computational fluid dynamics (CFD) methods, the LBE method is based on microscopic models and mesoscopic kinetic equations in which the collective behavior of the particle distribution function (PDF) is used to simulate the continuum mechanics of the system. Due to this kinetic nature, the LBE method has been found to be particularly useful in applications involving interfacial dynamics and phase transitions, e.g., multiphase or multicomponent flows, where traditional CFD methods of solving Navier-Stokes (N-S) equations are inappropriate, if not impossible.[3]

Several lattice Boltzmann (LB) multiphase fluid models were proposed in the past decade. The first immiscible LB model uses red- and blue-colored particles to represent two kinds of fluids.[4] The phase separation is then produced by the repulsive interaction based on the color gradient. The model proposed by Shan and Chen (SC) imposes the nonlocal interactions between fluid particles at neighboring lattice sites[5–7] by adding an additional forcing term to the velocity field. The potentials of the interaction control the form of the equation of state (EOS) of the fluid, and phase separation occurs automatically when the interaction potentials are properly chosen. There is also the so-called free-energy-based approach proposed by Swift *et al.*[8,9] In this model, the description of nonequilibrium dynamics, such as Cahn-Hilliard's approach, is incorporated into the LB model by using the concepts of the free-energy function. The free-energy-based model has a sound physical basis, and, unlike the SC model, the local momentum conservation is satisfied. However, this model does not satisfy Galilean invariance and some unphysical effects will be produced.[10] In the multiphase model proposed by He, Chen, and Zhang (HCZ),[11] two sets of PDFs are employed. The first PDF set is used to simulate pressure and velocity fields and another PDF set is used to capture the interface only, which makes this approach

essentially close to the interface capturing methods (such as the level set and volume-of-fluid methods) in spirit.

Despite the progress made by these models in simulating multiphase flows, there is a crucial missing part: the lack of a thorough investigation of incorporating different EOS into the LB model. The above-mentioned LB models are only tested for single and simple EOS, e.g., the free-energy-based model uses only the van der Waals (vdW) EOS and the HCZ model uses only the Carnahan-Starling (C-S) EOS. Furthermore, some important issues related to the numerical behavior of different EOS in the LB model, like the spurious current, coexistence curve, temperature range, etc., have not been properly addressed in the literature.

This paper focuses on the incorporation of various EOS in the SC LB model. We first briefly review the SC single-component multiphase model. Then we employ the original EOS proposed by SC to illustrate some important criteria used in evaluating the behavior of an EOS. Next, the simulation results are presented to compare different EOS in terms of the spurious current, density ratio, and temperature range. Furthermore, the coexistence curves obtained from the simulations are compared with the theoretical and experimental data for some typical EOS. The paper concludes with a discussion about the LBE method's applicability and perspectives in simulating multiphase flow with different EOS.

II. MODEL AND THEORY

A. Single-component multiphase lattice Boltzmann model

Our starting point is the standard LBE with the Bhatnagar-Gross-Krook (BGK) collision term (often referred to as the LBGK scheme), which describes the evolution of the PDF f_α in space **x** and time t,

$$f_\alpha(\mathbf{x} + \mathbf{e}_\alpha \delta t, t + \delta t) = f_\alpha(\mathbf{x}, t) - \frac{1}{\tau}[f_\alpha(\mathbf{x}, t) - f_\alpha^{eq}(\mathbf{x}, t)]$$

$$\alpha = 0, 1, \ldots, N, \tag{1}$$

where f_α is the PDF along the αth direction and f_α^{eq} is its corresponding equilibrium PDF, δt is the time step, $\mathbf{e}_\alpha$ is the

[a] Electronic mail: pengyuan@gmail.com

18, 042101-1

particle velocity in the αth direction, and τ is the single relaxation time. N is the number of discrete particle velocities.

The local mass density ρ and the local momentum density $\rho\mathbf{u}$ are obtained from

$$\rho = \sum_{\alpha=0}^{N} f_\alpha = \sum_{\alpha=0}^{N} f_\alpha^{\text{eq}}, \tag{2a}$$

$$\rho\mathbf{u} = \sum_{\alpha=0}^{N} f_\alpha \mathbf{e}_\alpha = \sum_{\alpha=0}^{N} f_\alpha^{\text{eq}} \mathbf{e}_\alpha, \tag{2b}$$

where $\mathbf{u}$ is the macroscopic velocity.

In LB simulations, the D2Q9 model with nine velocity directions on the two-dimensional (2D) square lattice has been widely used for 2D flow. For simulating three-dimensional (3D) flow, there are several cubic lattice models available, such as the D3Q15, D3Q19, and D3Q27 models. The equilibrium PDF for all of the D2Q9, D3Q15, D3Q19, and D3Q27 models can be expressed in the form

$$\mathbf{e}_\alpha = \begin{cases} (0,0,0), & \alpha=0; \\ (\pm 1,0,0)c, (0,\pm 1,0)c, (0,0,\pm 1)c, & \alpha=1,2,\ldots,6; \\ (\pm 1,\pm 1,0)c, (\pm 1,0,\pm 1)c, (0,\pm 1,\pm 1)c, & \alpha=7,8,\ldots,18. \end{cases} \tag{5a}$$

$$w_\alpha = \begin{cases} 1/3, & \alpha=0; \\ 1/18, & \alpha=1,2,\ldots,6; \\ 1/36, & \alpha=7,8,\ldots,18. \end{cases} \tag{5b}$$

The viscosity in the LBE model is given by

$$\nu = \left(\tau - \tfrac{1}{2}\right) c_s^2 \delta t, \tag{6}$$

where c_s is the lattice sound speed. This choice of the viscosity makes the LBGK scheme a second-order method for solving incompressible flow.[12]

Microscopically, the segregation of a fluid system into different phases is due to the interparticle forces. In the single-component multiphase LBE model proposed by SC, a simple long-range interaction force between the particles at site $\mathbf{x}$ and the particles at site $\mathbf{x}'$ is introduced,

$$\mathbf{F}_{\text{int}}(\mathbf{x}) = -\psi(\mathbf{x}) \sum_{\mathbf{x}'} G(\mathbf{x},\mathbf{x}') \psi(\mathbf{x}') (\mathbf{x}' - \mathbf{x}), \tag{7}$$

where $G(\mathbf{x},\mathbf{x}')$ is Green's function and satisfies $G(\mathbf{x},\mathbf{x}') = G(\mathbf{x}',\mathbf{x})$. It reflects the intensity of the interparticle interaction, with $G(\mathbf{x},\mathbf{x}') < 0$ representing attractive forces between particles. $\psi(\mathbf{x})$ is called the "effective mass" and is defined as a function of $\mathbf{x}$ through its dependency on the local density, $\psi(\mathbf{x}) = \psi[\rho(\mathbf{x})]$.

$$f_\alpha^{\text{eq}} = \rho w_\alpha \left[1 + \frac{3}{c^2} \mathbf{e}_\alpha \cdot \mathbf{u} + \frac{9}{2c^4} (\mathbf{e}_\alpha \cdot \mathbf{u})^2 - \frac{3}{2c^2} \mathbf{u} \cdot \mathbf{u} \right], \tag{3}$$

where w_α is the weighting factor, $c = \delta x / \delta t$ is the lattice speed, and δx is the lattice constant.

In this research, we use the D2Q9 and D3Q19 models for the 2D and 3D simulations, respectively. The weighting factor and discrete velocity for these two models are given below:

D2Q9:

$$\mathbf{e}_\alpha = \begin{cases} (0,0), & \alpha=0; \\ (\pm 1,0)c, (0,\pm 1)c, & \alpha=1,2,3,4; \\ (\pm 1,\pm 1)c, & \alpha=5,6,7,8. \end{cases} \tag{4a}$$

$$w_\alpha = \begin{cases} 4/9, & \alpha=0; \\ 1/9, & \alpha=1,2,3,4; \\ 1/36, & \alpha=5,6,7,8. \end{cases} \tag{4b}$$

D3Q19:

In order to perform the numerical simulation, SC introduced the concept of the nearest-neighbor interparticle force, which means that only the interactions between the nearest neighbors are considered,

$$G(\mathbf{x},\mathbf{x}') = \begin{cases} g, & |\mathbf{x}-\mathbf{x}'| \le c, \\ 0, & |\mathbf{x}-\mathbf{x}'| > c, \end{cases} \tag{8}$$

where c is the lattice spacing. Therefore,

$$\mathbf{F}_{\text{int}}(\mathbf{x}) = -\psi(\mathbf{x}) \sum_{\alpha=0}^{b} g\psi(\mathbf{x}+\mathbf{e}_\alpha)\mathbf{e}_\alpha. \tag{9}$$

In SC's original model, each lattice site has b nearest-neighboring sites with equal distance c and resides on a D dimensional space. $\mathbf{F}_{\text{int}}$ can be approximated by

$$\mathbf{F}_{\text{int}}(\mathbf{x}) \cong -\frac{c^2 b}{D} \psi(\mathbf{x}) g \nabla \psi(\mathbf{x}). \tag{10}$$

It should be noted here that although Eq. (10) is derived by using the interparticle forces of nearest-neighbor sites only in SC's original paper, it can be extended to include other neighboring sites as long as the gradient term $\nabla\psi(\mathbf{x})$ is properly specified. Therefore, for different lattice structures, Eq. (10) becomes

$$\mathbf{F}_{\text{int}}(\mathbf{x}) \cong -c_0 \psi(\mathbf{x}) g \nabla \psi(\mathbf{x}), \tag{11}$$

where c_0 is the constant depending on the lattice structure. For the D2Q9 and D3Q19 lattices, $c_0 = 6.0$, and for the D3Q15 lattice, $c_0 = 10.0$.

An example will be presented for the way to numerically evaluate the gradient term $\nabla \psi(\mathbf{x})$ in a D2Q9 lattice. Suppose we use both nearest and next-nearest sites to evaluate this gradient term, which gives a six-point scheme for two dimensions,

$$\frac{\partial \psi(i,j)}{\partial x} = c_1[\psi(i+1,j) - \psi(i-1,j)] + c_2[\psi(i+1,j+1)$$
$$- \psi(i-1,j+1) + \psi(i+1,j-1)$$
$$- \psi(i-1,j-1)],$$

$$\frac{\partial \psi(i,j)}{\partial y} = c_1[\psi(i,j+1) - \psi(i,j-1)] + c_2[\psi(i+1,j+1)$$
$$- \psi(i+1,j-1) + \psi(i-1,j+1)$$
$$- \psi(i-1,j-1)], \tag{12}$$

where c_1 and c_2 are weighting coefficients for nearest and next-nearest sites, respectively. For the second-order central difference scheme, $\partial \psi(i,j)/\partial x = \psi(i+1,j) - \psi(i-1,j)/2\Delta x$, since in the LBE method, $\Delta x = \Delta y = 1$. By averaging terms of next-nearest sites to nearest sites, we found that correct representation of the gradient term will require $c_1 + 2c_2 = 1/2$. Meanwhile, for the purpose of maintaining the isotropy of the scheme, the sites used in the calculation of the gradient term should be symmetric about the axes $x = i$ and $y = j$. Finally, we require that $c_1 > c_2$ since, physically, the closer sites will have more influence on the interaction.

Now we examine several schemes used in the literature. If we set $c_1 = 4c_2$, we found that this is essentially the "nearest and next-nearest scheme" used in Kang's paper,[13] where Eq. (7) is used and $G(\mathbf{x}, \mathbf{x}')$ is given by

$$G(\mathbf{x}, \mathbf{x}') = \begin{cases} g', & |\mathbf{x} - \mathbf{x}'| = 1, \\ g'/4, & |\mathbf{x} - \mathbf{x}'| = \sqrt{2}, \\ 0, & \text{otherwise.} \end{cases} \tag{13}$$

The only difference is that g' needs to be rescaled. Comparing Eqs. (7), (11), and (12), we find that

$$g' = c_0 c_1 g = 6 * \tfrac{1}{3} g = 2g. \tag{14}$$

If we set $c_1 = 2c_2$, we can recover another scheme used by Sukop.[14] Again, one only needs to rescale g' accordingly. Using Eq. (7), different forms of $G(\mathbf{x}, \mathbf{x}')$ were proposed in the literature,[15] which result in different critical values of g. However, by comparing them with Eq. (11), we can link all of these critical values together.

In calculating the gradient term, one can include more sites, but by doing so more weighting coefficients need to be added in Eq. (12). Determining these additional weighting coefficients is not straightforward. The "correct" scheme not only needs to satisfy the above-mentioned criteria, but also should generate the same density profiles for the flat interface case. The spurious currents (the unphysical velocities

generated in the simulation), isotropy, and stability of the scheme can differ considerably for different schemes, especially for the circular interface. We found that the 20-point scheme used in Qian's paper[16] gives the smallest spurious currents and better isotropy for the circular interface. However, this scheme is computationally more expensive than the six-point scheme (for the 3D case, it needs 44 neighboring sites) and is more complicated when dealing with the wall boundary. Therefore, in this paper we use the six-point scheme with $c_1 = 4c_2 = 1/3$ for the D2Q9 model, which can provide more isotropy simulation results for a circular interface than any of the other six-point schemes. Since the D2Q9 model can be viewed as a 2D projection of the D3Q19 model, if we proceed with the same projection for the gradient term, we will find the corresponding scheme in the D3Q19 model requires $c_1 = 2c_2 = 1/6$. The spurious currents produced by these two schemes are at the same level and are only slightly higher than that of 20-point scheme.

The interaction force can be incorporated into the model by shifting the velocity in the equilibrium distribution. That means the velocity $\mathbf{u}$ in Eq. (2) is replaced by

$$\mathbf{u}^{\text{eq}} = \mathbf{u} + \frac{\tau \mathbf{F}_{\text{int}}}{\rho(\mathbf{x})}. \tag{15}$$

Then, by averaging the moment before and after the collision, the whole fluid velocity $\mathbf{U}$ is

$$\rho(\mathbf{x})\mathbf{U} = \rho(\mathbf{x})\mathbf{u} + \tfrac{1}{2}\mathbf{F}_{\text{int}}. \tag{16}$$

There are also other approaches for incorporating the interaction force, such as direct body forcing, where the interaction is incorporated into the body force term of the Boltzmann equation by adding an additional term after the collision process.[17,18]

B. Criteria used in evaluating equations of state

Equations of state attempt to describe the relationship between temperature, pressure, and volume (or density) for a given substance or mixture of substances. If the interaction force is given by Eq. (11), then the EOS of the system is given by

$$p = c_s^2 \rho + \frac{c_0}{2} g[\psi(\rho)]^2, \tag{17}$$

where c_s is the speed of sound for the LB scheme. For the D2Q9 and D3Q19 models, $c_s = 1/\sqrt{3}$. If there is no interaction force, then the fluid will behave like an ideal gas. Theoretically, by changing the form of $\psi(\rho)$, different EOS can be obtained. However, after a thorough review of the literature, it appears that all of the papers using the SC model adopted only the EOS given in SC's original paper and no other EOS have been utilized. There is also a lack of thorough investigations of different EOS for other multiphase LB models. Therefore, it is worthwhile to study the performance of the SC model under different EOS.

In this section, we will use the EOS proposed by SC, referred to as the SC EOS hereafter, to demonstrate the criteria related to the evaluation of an EOS. For the SC EOS, the effective mass $\psi(\rho)$ is taken to be $\psi(\rho)$
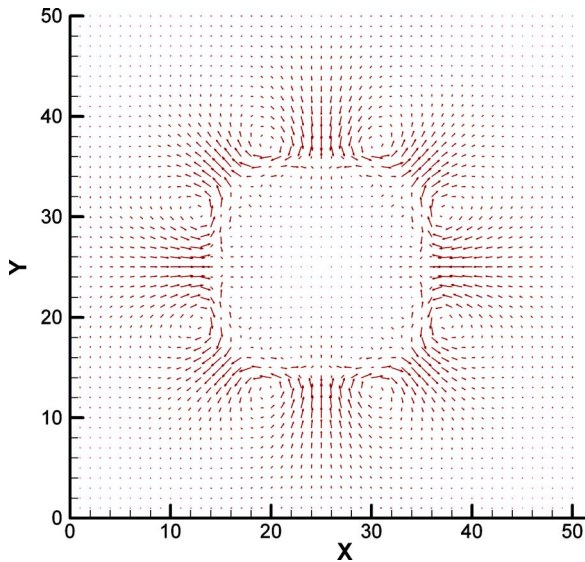
FIG. 1. (Color online) Velocity vectors plot in the xy plane at $z=25$ (symmetry plane).

FIG. 2. The maximum magnitude of spurious current changes with reduced temperature.

$=\rho_0[1-\exp(-\rho/\rho_0)]$. Therefore, the SC EOS is $p=\rho/3 +c_0/2g\rho_0^2[1-\exp(-\rho/\rho_0)]^2$, which gives a nonmonotonic pressure-density relationship. At the critical point, both first- and second-order pressure derivatives with respect to the density are zero, $(\partial p/\partial v)_T=(\partial^2 p/\partial v^2)_T=0$. So one can obtain the critical properties for the SC EOS as follows: $\rho_c =\rho_0 \ln 2$ and $g_c=-2/(9\rho_0)$. In the SC EOS, the role of temperature is dictated by g. We can define temperature in the SC EOS as $T=-1/g$, and the critical temperature becomes $T_c=-1/g_c=4.5\rho_0$. Hence for $g<g_c$, at a single pressure, two densities of the same material can coexist. However, to make phase separation occur, another condition must be satisfied also, i.e., $\rho_v<\bar{\rho}<\rho_l$, where ρ_v and ρ_l are the vapor and liquid densities at the specified temperature, and $\bar{\rho}$ is the average density of the whole system. This condition guarantees that the system is in the two-phase region. Otherwise the system is in the single-phase region and no phase separation will occur.

To illustrate the outcomes of this model, we now present some results of static bubble tests for a 3D single-component system. The $50\times50\times50$ lattice and periodical boundary conditions are used in all of the tests. Initially, a droplet with a radius of $r_{init}=10$ is placed at the center of the domain with the liquid (vapor) phase inside (outside) the droplet. Each test was run for 30 000 time steps. At that point, the relative differences of the maximum magnitudes of the velocities at time step t and $t-1000$ are on the order of 10^{-6}, which means that steady state is reached. A typical velocity field in the xy plane at the midpoint of $z=25$ is plotted in Fig. 1. The non-zero velocity vectors in Fig. 1 are the so-called spurious currents, denoted as $\mathbf{u}^s$ hereafter, and indicate the deviation from the real physical situation. These unphysical spurious currents reach their maximum value at the interface region.

Reducing the spurious currents is very important for the LB two-phase simulations for the following reasons. First, the LBE method is valid only in the incompressible limit $|\mathbf{u}|_{max}/c_s\rightarrow 0$, where $\mathbf{u}$ is the velocity of the system. If $|\mathbf{u}^s|_{max}$
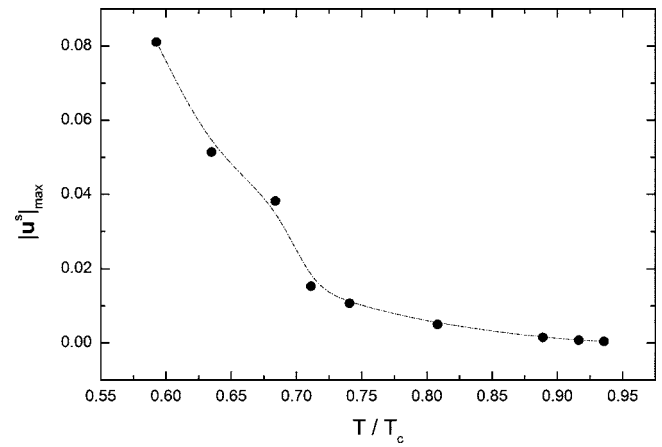
is too big, since we cannot separate spurious currents from real flow velocities, we therefore cannot get meaningful results. Second, large spurious currents will make the simulation unstable. Finally, we have proposed a thermal two-phase flow model based on the SC model,[19] where the flow velocity was taken as the advection velocity of the temperature field. Therefore, a more accurate velocity field is required in order to calculate an accurate temperature field. The previous research showed that the temperature field has some fluctuations near the interface region where the magnitudes of the spurious currents are higher than at any other place. If we can lower the spurious currents, we therefore can lower these fluctuations and obtain better local temperature distributions.

For comparison, we also simulated a two-phase system with a flat interface. In this case, the $|\mathbf{u}^s|_{max}$ is much smaller —on the order of 10^{-14}. In this paper we will investigate the spurious current levels for circular interfaces under different EOS, because the circular interface is more often encountered in real applications. Furthermore, even if the interface is undergoing some deformations and becomes no longer circular, the $|\mathbf{u}^s|_{max}$ stays at the same level, as has been verified in the simulations.[19] Therefore, in this research, we only test the no-flow (static) case and compare the corresponding spurious current level for different EOS. The spurious currents for the dynamic case are expected to be at the same level and their effect on fluid dynamics will be studied in the future.

Besides the spurious currents, other important issues related to evaluating an EOS are the stable temperature range, the coexistence curve, and the density ratio. We briefly discuss these criteria next, and then compare their values for various EOS in Sec. III.

Ideally, one wants a two-phase model that can handle the entire two-phase region, which is from the triple point to the critical point. However, as the temperature decreases in the two-phase region, the density ratio increases and the surface tension also increases. The overall effect results in higher spurious currents (we defer the details of this discussion to a future publication). Therefore, at a certain temperature, the spurious currents become so high as to make the scheme unstable. Figure 2 shows the $|\mathbf{u}^s|_{max}$ as a function of reduced

temperature (T/T_c) for the SC EOS. We define the lowest temperature which maintains stability as $T_{\min}$ and compare these temperatures under different EOS.

It was argued that a serious limitation of the SC model is that one cannot introduce a well-defined temperature, which is consistent with thermodynamics, into the model. This is because the Maxwell equal-area construction is not satisfied except for one special form of the effective mass, $\psi(\rho) = \psi_0 \exp(-\rho_0/\rho)$, where ψ_0 and ρ_0 are arbitrary constants. Therefore, to address the applicability of the SC model, it is important to check the deviation of the coexistence curve obtained from the simulation from the theoretical one that is predicted by the Maxwell equal-area construction.

Finally, in reality for a vapor-liquid two-phase system, the density ratio between the liquid and vapor phases can easily be over 100:1. However, it is difficult for most LB schemes to deal with two phases with a high density ratio. For example, as reported in Swift's paper, the density ratio obtained using the free-energy-based approach is less than 10:1, and the largest density ratio tested in the HCZ approach is 40:1. Since spurious currents are ubiquitous in the S-C model (as well as in many other models), increasing the density ratio will always result in an increase in the spurious current and finally make the simulation unstable. We found that by changing the EOS, one can reach density ratios higher than 1000:1 with the simulation still stable. We will compare the achievable density ratios for different EOS accordingly.

C. Incorporating equations of state

In this paper, we will compare the following EOS:

(i)   SC,
(ii)   vdW,
(iii)   Redlich-Kwong (R-K),
(iv)   Redlich-Kwong Soave (RKS),
(v)   Peng-Robinson (P-R), and
(vi)   Carnahan-Starling (C-S).

Except for the SC and C-S EOS, all of the other EOS are cubic in form. Furthermore, the vdW and R-K EOS are two-parameter EOS, while the RKS and P-R EOS are three-parameter EOS.

The vdW EOS is the simplest and yet most famous cubic EOS. Although other modern EOS of only slightly greater complexity are much more accurate than the vdW EOS, we include it here to demonstrate some important concepts.

The vdW EOS is

$$p = \frac{\rho R T}{1 - b\rho} - a\rho^2, \tag{18}$$

where a is the attraction parameter and b is the repulsion parameter.

From Eq. (17), we find that for any given EOS, the corresponding effective mass can be written as

$$\psi(\rho) = \sqrt{\frac{2(p - c_s^2\rho)}{c_0 g}} = \sqrt{\frac{2p^*}{c_0 g}}, \tag{19}$$

where $p^* = p - c_s^2\rho$ is the nonideal part of the EOS. Substituting Eq. (18) into Eq. (19), we get

$$\psi(\rho) = \sqrt{\frac{2\rho\left(\dfrac{RT}{1 - b\rho} - a\rho - c_s^2\right)}{c_0 g}}. \tag{20}$$

The g value becomes unimportant in this case, because unlike in the SC EOS, we have a defined temperature in the vdW EOS. When calculating the interaction force and pressure using Eqs. (11) and (17), g is canceled out. The only requirement for g is to ensure that the whole term inside the square root is positive. This argument holds for other EOS also if the temperature is not a function only of g.

For the vdW EOS, the critical properties are given by

$$\rho_c = \frac{1}{3b}, \quad p_c = \frac{a}{27b^2}, \quad T_c = \frac{8a}{27Rb}. \tag{21}$$

In our simulations, we set $a = 9/49$, $b = 2/21$, and $R = 1$. Then the critical density is $\rho_c = 7/2$ and the critical temperature is $T_c = 4/7$, both of which are in lattice units. In an effort to relate these values to the real physical properties, we use the concept of reduced properties,[20]

$$\rho_R = \frac{\rho}{\rho_c}, \quad p_R = \frac{p}{p_c}, \quad T_R = \frac{T}{T_c}, \tag{22}$$

where the subscripts "R" and "c" denote the reduced and critical properties, respectively. According to the law of corresponding states, the reduced properties should be the same no matter what kind of units are used, therefore, $\rho_R = \rho^{Lu}/\rho_c^{Lu} = \rho^{\mathrm{real}}/\rho_c^{\mathrm{real}}$, which gives $\rho^{\mathrm{real}} = \rho^{Lu}\rho_c^{\mathrm{real}}/\rho_c^{Lu}$. Similarly, $p^{\mathrm{real}} = p^{Lu}p_c^{\mathrm{real}}/p_c^{Lu}$ and $T^{\mathrm{real}} = T^{Lu}T_c^{\mathrm{real}}/T_c^{Lu}$, where the superscripts "real" and "Lu" denote real units and lattice units, respectively. In this way, one can easily convert a lattice property to a real property. The other EOS used in this paper are given below:

R-K EOS:

$$p = \frac{\rho R T}{1 - b\rho} - \frac{a\rho^2}{\sqrt{T}(1 + b\rho)}, \tag{23}$$

with $a = 0.427\,48 R^2 T_c^{2.5}/p_c$, $b = 0.086\,64 R T_c/p_c$.

RKS EOS:

$$p = \frac{\rho R T}{1 - b\rho} - \frac{a\alpha(T)\rho^2}{1 + b\rho}, \tag{24}$$

$$\alpha(T) = [1 + (0.480 + 1.574\omega - 0.176\omega^2)(1 - \sqrt{T/T_c})]^2, \tag{25}$$

with $a = 0.427\,48 R^2 T_c^2/p_c$, $b = 0.086\,64 R T_c/p_c$.

P-R EOS:

$$p = \frac{\rho R T}{1 - b\rho} - \frac{a\alpha(T)\rho^2}{1 + 2b\rho - b^2\rho^2}, \tag{26}$$

$$\alpha(T) = [1 + (0.374\,64 + 1.542\,26\omega - 0.269\,92\omega^2)$$
$$\times (1 - \sqrt{T/T_c})]^2, \tag{27}$$

with $a = 0.457\,24R^2T_c^2/p_cb = 0.0778RT_c/p_c$.

C-S EOS:

$$p = \rho RT \frac{1 + b\rho/4 + (b\rho/4)^2 - (b\rho/4)^3}{(1 - b\rho/4)^3} - a\rho^2, \tag{28}$$

with $a = 0.4963R^2T_c^2/p_c$, $b = 0.187\,27RT_c/p_c$.

In the above EOS, R-K, RKS, and P-R are classified as cubic EOS. As mentioned previously, the R-K EOS is a two-parameter EOS, using two parameters (T_c, p_c); the RKS and P-R EOS are three-parameter EOS, with an additional parameter ω, which is the acentric factor. This additional parameter gives us some flexibility in modeling different fluids. For all of these cubic EOS, we set $a = 2/49$, $b = 2/21$, and $R = 1$ in our simulations. The C-S EOS is different from the above cubic EOS in that it modifies the hard sphere term of the vdW EOS, while all of the other cubic EOS modify the attraction term of the vdW EOS. For the C-S EOS, we set $a = 1$, $b = 4$, and $R = 1$ in our simulations.

III. SIMULATION RESULTS AND DISCUSSION

In this section, we first compare the simulation results of three types of EOS, i.e., the SC, vdW, and C-S. Next, we compare the simulation results of all of the cubic EOS. Finally, we will compare our simulation results with some real fluid data.

A. Comparison of different types of equations of state

Figure 3 shows the variation of $|\mathbf{u}^s|_{max}$ with the density ratio for the vdW EOS, which is close to a linear relation. The lowest temperature we can reach is $T_{min} = 0.445 = 0.778\,75T_c$, and the scheme becomes unstable with temperatures lower than that.

Figure 4 shows $|\mathbf{u}^s|_{max}$ changing with the density ratio for the SC and C-S EOS. The inset diagram shows the $|\mathbf{u}^s|_{max}$ variation for density ratios smaller than 50. As can be seen from the inset, for a given density ratio, the C-S EOS generates much smaller spurious currents than the SC EOS. Furthermore, the C-S EOS provides a larger range of density ratios; e.g., when the density ratio equals 103.74, $|\mathbf{u}^s|_{max}$ for the C-S EOS is only 1.74E-02, while for the SC EOS, when the density ratio equals 58.497, $|\mathbf{u}^s|_{max}$ already reaches 8.11E-02. The critical temperature for the C-S EOS is $T_c = 0.3773a/bR$. Therefore, the lowest temperature we can achieve for the C-S EOS is $T_{min} = 0.2a/bR = 0.53T_c$, which is much lower than that of the vdW EOS.

In Table I, we compare the properties at T_{min} for different EOS. We can see that at T_{min}, the $|\mathbf{u}^s|_{max}$ for vdW EOS is much smaller than that of the SC EOS and C-S EOS. We believe that unlike the other two EOS, where instability results from large spurious currents, for the vdW EOS, the
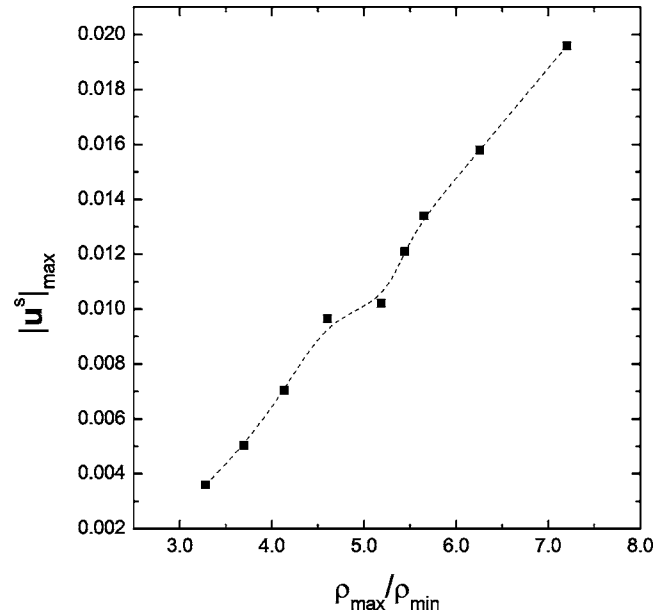
FIG. 3. The maximum magnitude of spurious current changes with density ratio.

instability comes from the EOS itself. Therefore, the vdW EOS is not suitable for a vapor-liquid system with temperatures much lower than the critical one. However, by replacing the vdW EOS with a more realistic modified form such as the C-S EOS, we will get a much better performance with a wider temperature range, higher density ratio, and much smaller spurious currents. Furthermore, by using C-S EOS the simulation is still stable when density ratio reaches 1000, although the spurious current is high at this stage. If one restrains the spurious current to be smaller than 0.02 in the simulation, the corresponding density ratio for the S-C EOS is around 25.6, but for C-S EOS is around 124.6, which is 4.86 times higher than that of the S-C model.
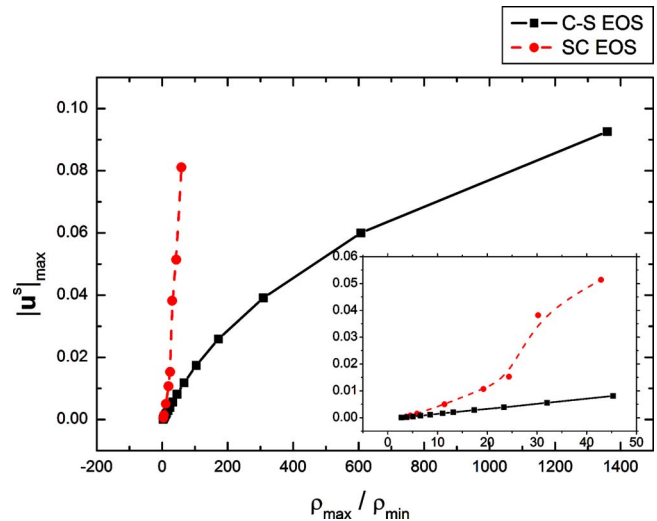
FIG. 4. (Color online) Maximum magnitude of spurious current changes with density ratio for the SC and C-S EOS.

TABLE I. Properties at T_{min} for different EOS.

EOS	Critical temperature (T_c)	T_{min}/T_c	$|\mathbf{u}^s|_{max}$	ρ_{max}/ρ_{min}
SC	4.5	0.592 59	0.0811	58.497 53
vdW	4/7	0.778 75	0.019 599	7.202 862
C-S	0.3773a/bR	0.5301	0.092 571	1359.497

B. Comparison of different cubic equations of state

Since the C-S EOS, which is a modification of the vdW EOS, has a much better performance in simulating two-phase flow than the original vdW EOS, we now consider another way of modifying the vdW EOS, i.e., modifying the attraction term of the vdW EOS, which results in several cubic EOS.

Figure 5 gives the $|\mathbf{u}^s|_{max}$ changes with the density ratio for different cubic EOS. For the RKS and P-R EOS, we set $\omega=0.344$, which is the acentric factor of water.

From Fig. 5, we can see that at the same density ratio, all of the modified EOS have smaller $|\mathbf{u}^s|_{max}$ values than the vdW EOS. The $|\mathbf{u}^s|_{max}$ of the P-R EOS is even smaller than that of the C-S EOS. The P-R EOS can also handle a density ratio as high as 1000, with $|\mathbf{u}^s|_{max}=0.069\,02$ when density ratio equals 905.9411. The $|\mathbf{u}^s|_{max}$ for the R-K EOS and RKS EOS are close to each other at lower density ratios. When density ratio is higher than 50, the R-K EOS gives a smaller $|\mathbf{u}^s|_{max}$.

Figure 6 gives the coexistence curves obtained from the simulations for the various EOS. The coexistence curves of the RKS and P-R EOS are quite close, which is to be expected, since we use the same acentric factor for these two EOS. However, the P-R EOS can utilize a wider temperature range than the RKS EOS, because the P-R EOS has a much smaller $|\mathbf{u}^s|_{max}$ under the same density ratio. The smallest reduced temperature (T_{min}/T_c) is 0.649 20, 0.782 52, and 0.587 71 for the R-K, RKS, and P-R EOS, respectively.

We noticed that in order to achieve a high density ratio, Inamuro[21,22] and Lin[23,24] recently proposed different approaches. Both of their models are essentially single-component two-phase models and two sets of particle distribution functions were used in these two approaches, which makes them computationally more expensive than our method. Inamuro's approach is based on Swift's free-energy-based model and uses the projection method[25] to achieve a high density ratio. In his approach, two sets of PDFs, one for the order parameter and the other for the predicted velocity of the two fluids without a pressure gradient, were used. The pressure correction is then added into the model by solving the pressure Poisson equation using an iteration method, which further undermines the simplicity of the LBE method. In Lin's approach, in order to stabilize the scheme, the collision step has been split into pre- and poststreaming collision steps and the forcing terms in these two steps must be treated differently, which also increases computational loads. Although density ratios up to 1000 can be achieved in both methods, classified as diffuse interface methods, none of these methods eliminates the spurious current. In Inamuro's
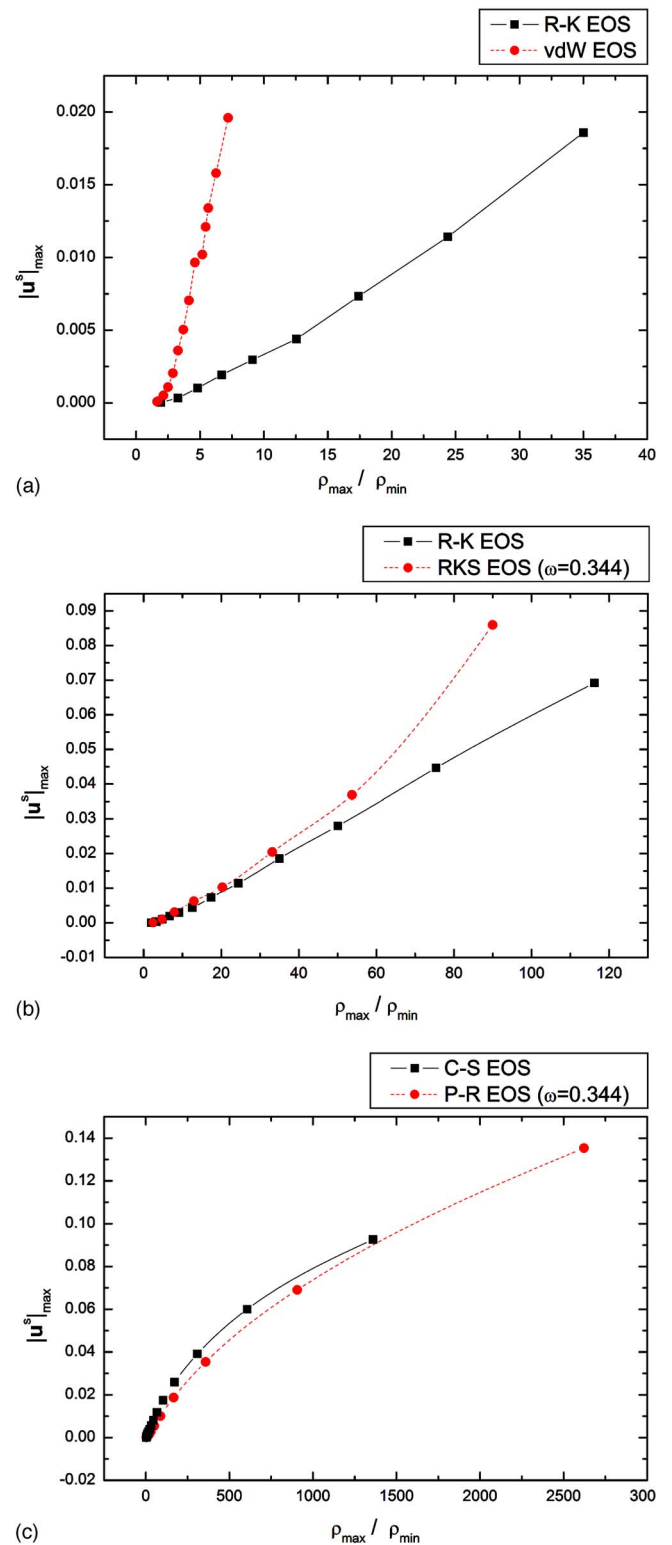

FIG. 5. (Color online) The maximum magnitude of spurious current changes with density ratio for different EOS. (a) Comparison between the vdW and R-K EOS. (b) Comparison between the R-K and RKS EOS. (c) Comparison between the P-R and C-S EOS.

approach, the magnitude of spurious current was given for a density ratio of 50, which is at the same level of spurious current generated using S-C's original EOS. Lin's approach has a better performance in terms of spurious current. In Lin's approach, by introducing chemical potential, the inter-
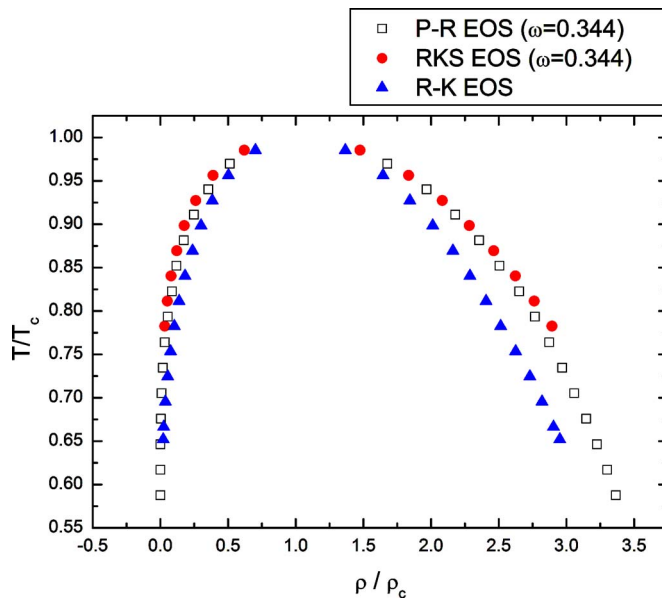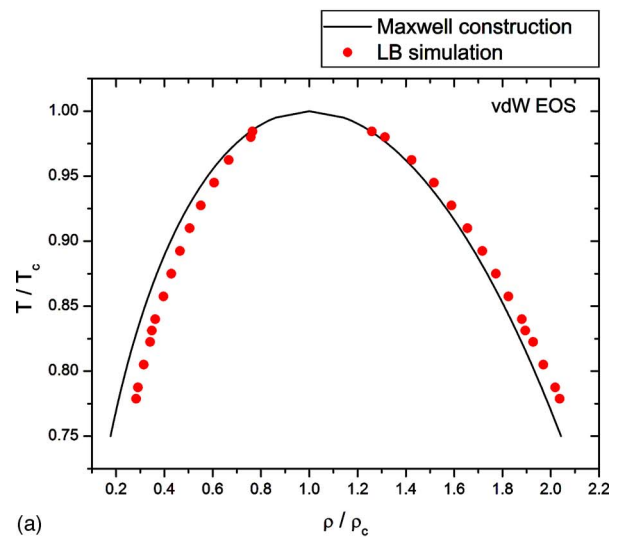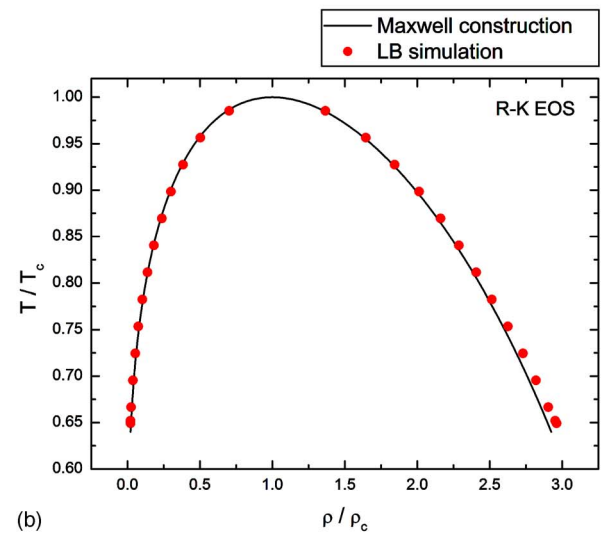
FIG. 6. (Color online) Coexistence curves obtained from simulations for different EOS.

face thickness and surface tension at equilibrium are controllable, which makes it more flexible than the S-C model. However, compared with their model, our approach is easier to implement in a range of situations since only the EOS needs to be changed.

It is also useful to evaluate these EOS by comparing the coexistence curves obtained from the simulations with the theoretical curves predicted by the Maxwell equal-area construction. This comparison is given in Fig. 7. From Fig. 7(a), we can see that the simulated coexistence curve for the vdW EOS deviated remarkably from the theoretical values, especially at low temperatures. At T_{min}, the relative error of the density, i.e., $|\rho_{LB} - \rho_{exact}|/\rho_{exact}$, for the liquid branch is 2.813% and for the vapor branch is 33.83%. As can be seen from Figs. 7(b) and 7(c), for the R-K and P-R EOS, the simulated coexistence curves fit well with the theoretical values. At T_{min}, the relative error of density for the liquid branch is less than 2%. However, for vapor branch, the relative error of the density can be quite big, although the absolute difference is very small. This is due to the nature of the EOS, since when the temperature is much lower than the critical temperature, the density ratio becomes quite high. For the P-R EOS, the density ratio can be higher than 1000, where even very small changes in the liquid density can cause large fluctuations of the vapor density. For this reason, we plot the coexistence curve of the vapor branch separately for the R-K EOS and P-R EOS in Figs. 8(a) and 8(b). We can see, although the coexistence curves deviated from the theoretical values, the trends of density changing with temperature are the same. Figure 9 shows the coexistence curve of C-S EOS and the theoretical one obtained by equating the chemical potentials. Again, good agreement is obtained. For P-R EOS, the acentric factor can also be specified to fit the real fluid properties. Figure 10 gives the coexistence curve of the P-R EOS for $\omega = 0.011$, which is the acentric factor of methane.
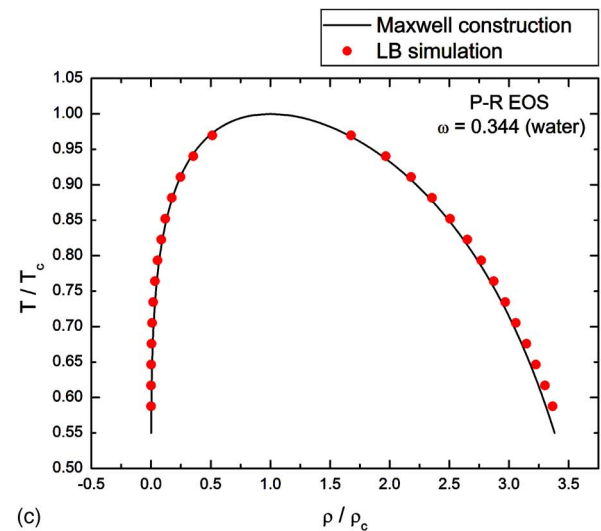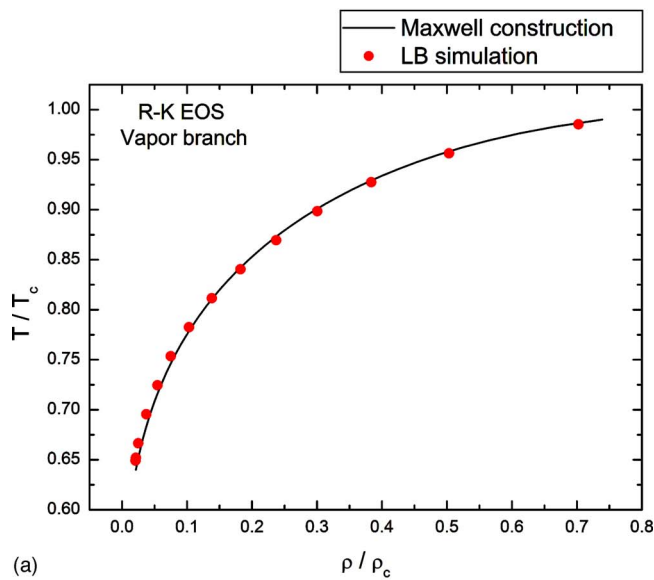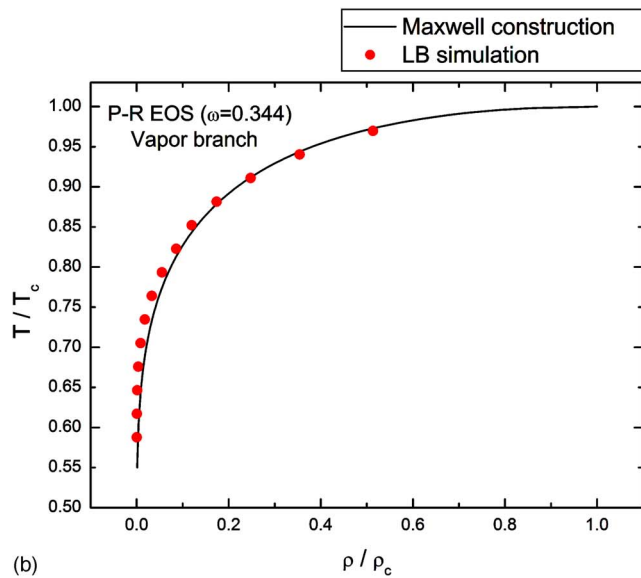

FIG. 7. (Color online) Comparison of coexistence curves obtained from simulations with theoretical values for different EOS: (a) Coexistence curve of the (a) vdW, (b) R-K, and (c) P-R EOS.

C. Comparison of equations of state and actual fluid properties

Finally, we compare our simulation results with some real fluid data. We chose the most commonly used fluid (wa-
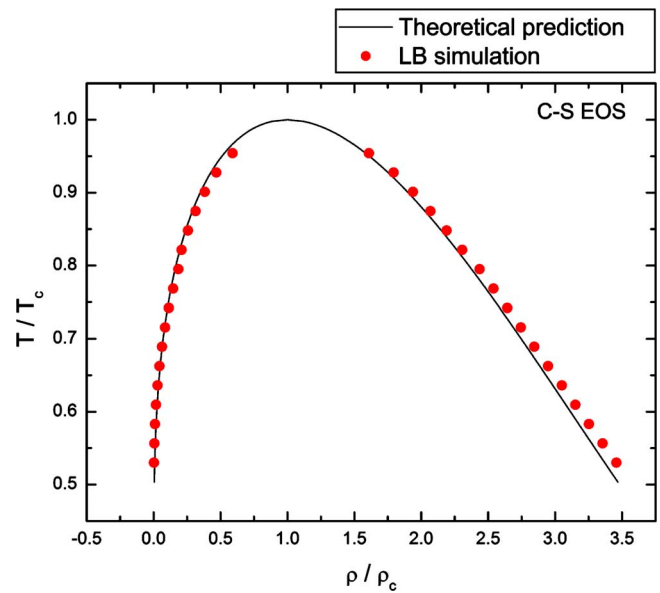
FIG. 9. (Color online) Comparison of coexistence curves obtained from simulations with theoretical values obtained by equating the chemical potentials for C-S EOS.

FIG. 8. (Color online) Comparison of the vapor branch of the coexistence curves obtained from simulations with theoretical values for R-K and P-R EOS. Vapor branch of the coexistence curve of the (a) R-K and (b) P-R EOS.

ent fluids. For example, by setting $\omega=0.011$, we are essentially using the properties of methane. The simulated coexistence curve for this value of the acentric factor is given in Fig. 10, and fits well with the theoretical values.

IV. DISCUSSION

It has been argued that a serious problem of the SC model is that one cannot introduce a thermodynamically well-defined temperature. However, from our simulations, we can see that by properly choosing the EOS, one can introduce temperature explicitly (in the SC EOS, there is indeed no explicitly defined temperature), and also have a coexistence curve very close to the theoretical prediction, which is thermodynamically well defined.

ter) in this case. The acentric factor for water is 0.344. Figure 11 gives the comparison of the saturated density obtained from simulations for the R-K and P-R EOS with the experimental data from the steam table. From this comparison with experimental data, we can see that for the liquid density, the R-K EOS gives better results, while for the vapor density, the P-R EOS gives better results. At T_{min}, the relative error of the liquid density is 11.815% for the P-R EOS. However, we still generally consider the P-R EOS to be superior to the R-K EOS because the P-R EOS allows for a wider temperature range and can handle higher density ratios. Furthermore, unlike the P-R EOS, the R-K EOS is a two-parameter EOS. Therefore, no matter what fluid is being simulated, it gives the same coexistence curve for the reduced properties. P-R EOS is a three-parameter EOS, and the third parameter (the acentric factor) gives us more flexibility in simulating differ-
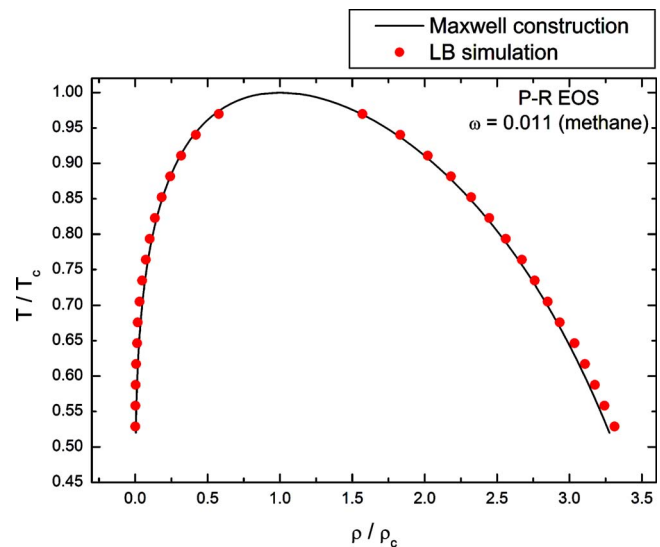

FIG. 10. (Color online) Comparison of coexistence curves obtained from simulations with theoretical values for P-R EOS with $\omega=0.011$.
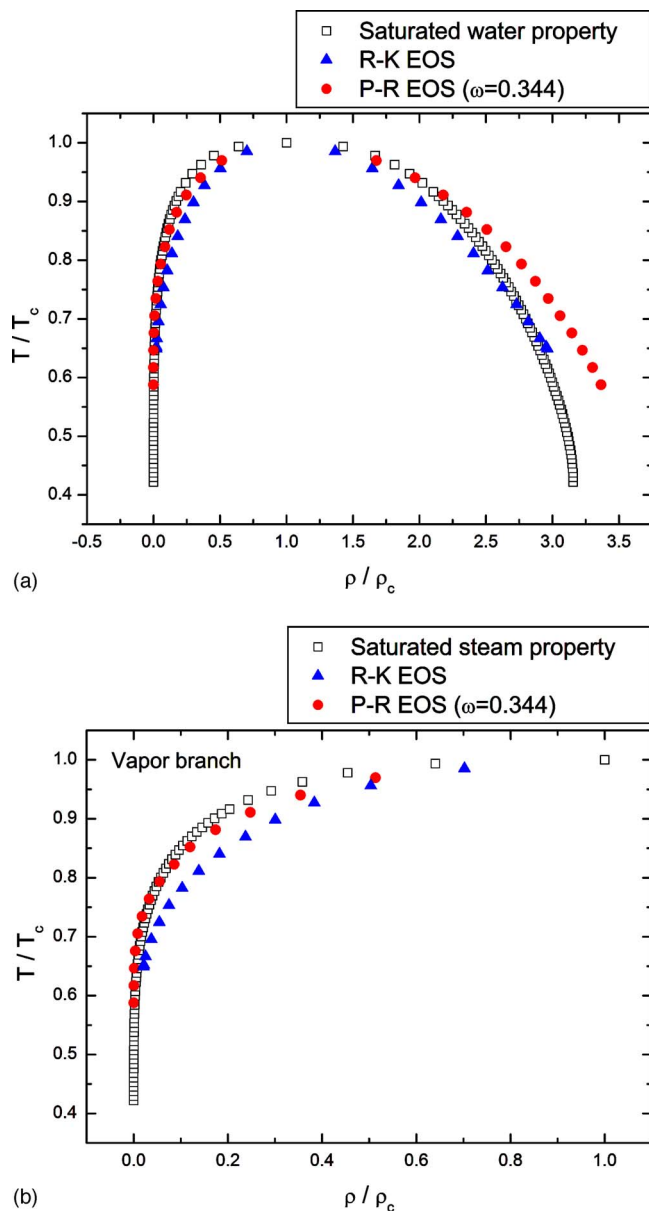
FIG. 11. (Color online) Comparison of the saturated density of water obtained from simulations with experimental data from the steam table for different EOS: (a) Vapor and liquid branch; (b) vapor branch.

In this paper, we have demonstrated the applicability of the LBE method in simulating two-phase flow using a variety of EOS. While suitable for some applications, the vdW EOS generally does not give satisfactory results. However, the C-S and P-R EOS, which are revisions of the vdW EOS for the hard sphere term and attraction term, respectively, demonstrate much better performance in terms of spurious currents, temperature ranges, and density ratios. Other revisions, such as the R-K and RKS EOS, also give better simulation results. Therefore, we can say that as the selected EOS becomes more realistic, a better performance will be obtained from the LBE simulation.

For the coexistence curves, the simulation results of the vdW EOS significantly deviate from the theoretical values. The simulation results of the R-K, P-R, and C-S EOS fit quite well with the theoretical values, however. Therefore, by properly choosing an EOS, we can both introduce temperature explicitly and develop a coexistence curve very close to the theoretical prediction.

Furthermore, by comparing the simulation results with experiment data for saturated water/steam, the R-K EOS gives better results for the water density and the P-R EOS gives better results for the steam density. There is a noticeable difference, particularly for the liquid leg, but this is due to the EOS itself, since the coexistence curve obtained from the simulation fits well with theoretical values. Therefore, a translation from the simulation results might be needed in this case. For future research, an investigation of other more realistic EOS, such as those with corrections for both the attraction and hard sphere terms of the vdW EOS, is very promising (as well as computationally challenging), and can greatly enlarge the applicability of the LBE method in two-phase flow simulation.

ACKNOWLEDGMENT

[1]S. Chen and G. D. Doolen, "Lattice Boltzmann method for fluid flows," Annu. Rev. Fluid Mech. **30**, 329 (1998).

[2]S. Succi, *The Lattice Boltzmann Equation for Fluid Dynamics and Beyond* (Oxford University Press, Oxford, UK, 2001).

[3]S. Hou, X. Shan, Q. Zou, G. D. Doolen, and W. Soll, "Evaluation of two lattice Boltzmann models for multiphase flows," J. Comput. Phys. **138**, 695 (1997).

[4]S. Chen, H. Chen, D. Martinez, and W. Matthaeus, "Lattice Boltzmann model for simulation of magnetohydrodynamics," Phys. Rev. Lett. **67**, 3776 (1991).

[5]X. Shan and H. Chen, "Lattice Boltzmann model for simulation flows with multiple phases and components," Phys. Rev. E **47**, 1815 (1993).

[6]X. Shan and H. Chen, "Simulation of nonideal gases and liquid-gas phase transitions by the lattice Boltzmann equation," Phys. Rev. E **49**, 2941 (1994).

[7]X. Shan and G. D. Doolen, "Multicomponent lattice-Boltzmann model with interparticle interaction," J. Stat. Phys. **81**, 379 (1995).

[8]M. Swift, W. Osborn, and J. Yeomans, "Lattice Boltzmann simulation of nonideal fluids," Phys. Rev. Lett. **75**, 830 (1995).

[9]M. Swift, S. Orlandini, W. Osborn, and J. Yeomans, "Lattice Boltzmann simulations of liquid-gas and binary-fluid systems," Phys. Rev. E **54**, 5041 (1996).

[10]R. Nourgaliev, T. Dinh, T. Theofanous, and D. Joseph, "The lattice Boltzmann equation method: Theoretical interpretation, numerics and implications," Int. J. Multiphase Flow **29**, 117 (2003).

[11]R. Zhang, "Lattice Boltzmann approach for immiscible multiphase flow," Ph.D. thesis, University of Delaware, 2000.

[12]X. He and L.-S. Luo, "Theory of the lattice Boltzmann method: From the Boltzmann equation to the lattice Boltzmann equation," Phys. Rev. E **56**, 6811 (1997).

[13]Q. Kang, D. Zhang, and S. Chen, "Displacement of a two-dimensional immiscible droplet in a channel," Phys. Fluids **14**, 3203 (2002).

[14]M. Sukop and D. Or, "Lattice Boltzmann method for modeling liquid-vapor interface configurations in porous media," Water Resour. Res. **40**, W01509 (2004).

[15]C. Pan, "Use of pore-scale modeling to understand flow and transport in porous media," Ph.D. thesis, University of North Carolina at Chapel Hill, 2003.

[16]D. Qian, "Bubble motion, deformation, and breakup in stirred tanks," Ph.D. thesis, Clarkson University, New York, 2003.

[17]J. Buick and C. Greated, "Gravity in the lattice Boltzmann model," Phys. Rev. E **61**, 5307 (2000).

[18] N. S. Martys and H. Chen, "Simulation of multicomponent fluids in complex three-dimensional geometries by the lattice Boltzmann method," Phys. Rev. E **53**, 743 (1996).

[19] P. Yuan and L. Schaefer, "Lattice Boltzmann simulation of two-phase flow and heat transfer in a rectangular channel," in Proceedings of the 2004 ASME International Mechanical Engineering Congress (Fluids Engineering Division), Anaheim, California, 2004, Vol. 463.

[20] D. McQuarrie and J. D. Simon, *Molecular Thermodynamics* (University Science, Sausalito, CA, 1999).

[21] T. Inamuro, T. Ogata, and F. Ogino, "Numerical simulation of bubble flows by the lattice Boltzmann method," FGCS, Future Gener. Comput. Syst. **20**, 959 (2004).

[22] T. Inamuro, T. Ogata, and F. Ogino, "A lattice Boltzmann method for incompressible two-phase flows with large density differences," J. Comput. Phys. **198**, 628 (2004).

[23] T. Lee and C.-L. Lin, "A stable discretization of the lattice Boltzmann equation for simulation of incompressible two-phase flows at high density ratio," J. Comput. Phys. **206**, 16 (2005).

[24] T. Lee and C.-L. Lin, "Pressure evolution lattice-Boltzmann-equation method for two-phase flow with phase change," Phys. Rev. E **67**, 056703 (2003).

[25] A. J. Chorin, "Numerical solution of the Navier-Stokes equations," Math. Comput. **22**, 745 (1968).